Hindawi
Mobile Information Systems
Volume 2022, Article ID 6091352, 15 pages
https://doi.org/10.1155/2022/6091352

*Research Article*

# Scientific Computational Visual Analysis of Wood Internal Defects Detection in View of Tomography Image Reconstruction Algorithm

**Ruochen Ye,[1] Ying Pei,[2] Weibin Wang,[1] and Haibin Zhou[3]**

[1]*Shanxi Academy of Ancient Building and Painted Sculpture & Fresco Preservation, Taiyuan, Shanxi, China 030012*
[2]*Shanxi Museum, Taiyuan, Shanxi, China 030000*
[3]*Chinese Academy of Forestry, Beijing, China 100000*

Correspondence should be addressed to Haibin Zhou; zhouhb@caf.ac.cn

Received 20 January 2022; Revised 1 March 2022; Accepted 7 March 2022; Published 27 March 2022

Academic Editor: Hye-jin Kim



With the development of non-destructive testing technology and computer technology, wood non-destructive testing technology will develop towards intelligence and automation. The primary condition for development is to be able to carry out the testing of various physical properties of wood without destroying the wood itself. Wood defects refer to abnormal wood structure. Its existence will affect the quality of wood, change the normal performance of wood, and reduce the utilization rate and use value of wood. The purpose of this article is to try to find an effective detection method without damaging the original structure of the wood. It can accurately and quickly determine the defect information on the wood surface. This research mainly discusses the visual analysis of wood internal defect detection based on tomographic image reconstruction algorithm. According to the analysis of the planks to be tested, this paper determines the structural characteristics, the types of defects to be tested, and the classification standards. To analyze the principle of machine vision imaging, this paper designs a hardware experiment system for wood board imaging, by observing the collected Biyun Temple building wood images and summarizing the Biyun Temple building wood defects, surface texture features, and various appearance features in the image. Based on digital image processing technology, this paper designs a complete set of real-time timber classification and detection algorithms. The algorithm realizes the extraction of Biyun Temple's architectural wood region, texture region extraction, and the comprehensive feature vector extraction of Biyun Temple's architectural wood. In the image preprocessing stage, the color image is converted into a grayscale image through the grayscale processing of the image. Through the equalization processing of the histogram, the defect features in the defect image are highlighted. Through image smoothing and denoising processing, the noise points that may exist in the image are removed. The signal-to-noise ratio of the Marching Cube algorithm is maintained at a relatively high level under different noise conditions, which is about 3-4db higher than the Gaussian method with OPED. This research is helpful for the continuation and inheritance of ancient architectural attainments.

## 1. Introduction

Non-destructive testing is based on the premise that it does not damage or affect the performance of the tested object and does not damage the internal organization of the tested object in the inspection of mechanical materials. It utilizes the changes in the reaction of heat, sound, light, electricity, magnetism, etc. caused by the abnormal or defective internal structure of the material, by means of physical or chemical methods, with the help of modern technology and equipment. It is a method for inspecting and testing the internal and surface structure, state, and defect type, quantity, shape, nature, location, size, distribution, and changes of the test piece. Wood identification is a task with high practical requirements. The earliest identification method must be completed by professionals with rich practical experience and professional theoretical knowledge. In ICT non-destructive testing, a slice of a certain part of the component can be obtained,

and a set of parallel two-dimensional slices can be obtained through multiple parallel scans. The defect can be found by observing this set of parallel two-dimensional tomographic images.

With the popularization and development of tomography equipment, coupled with the continuous improvement of the image resolution of imaging equipment, it can provide scientific visualization technology with tomographic images with smaller and smaller scanning distances. It makes the data rich and accurate in image reconstruction. The organic combination of the fast processing speed of the computer and the scanning equipment realizes the technology of computer-assisted surgery and simulation. It makes the 3D visualization technology have broad prospects in application.

Using computer vision methods, the information characteristics of wood images can be extracted, and then the model can be constructed to complete the recognition task. Chung, J. believes that due to patient movement or incorrect equipment calibration, it is inevitable in many imaging modes. For example, photoacoustic tomography (PAT) of a rotating system, if ignored, may cause undesirable motion artifacts in image reconstruction. He built a hybrid model for PAT, which added motion to the model. He introduced an approximate continuous model and established two unique results for some specific parametric motion models. Then, he expressed the discrete problem of simultaneous motion estimation and image reconstruction as a separable nonlinear least squares problem, and described an automatic method to detect and eliminate motion artifacts in the reconstruction process. Numerical examples verify his method [1]. Ramos, T. believes that X-ray computed tomography (CT) is a 3D imaging technique. It uses X-ray illumination and image reconstruction technology to reproduce the internal cross-section of the sample. Tomography projection data usually requires initial relative alignment or knowledge of the exact position and orientation of the object relative to the detector. With the increasing resolution of tomographic imaging, mechanical instability and equipment limitations are becoming the main leading factors leading to uncertainty in sample positioning. These factors will further introduce reconstruction artifacts and limit the resolution obtained in the final tomographic reconstruction. Alignment algorithms that require manual interaction hinder data analysis, and data collection rates continue to increase, and data collection rates are provided by better sources. He proposed an iterative reconstruction algorithm for wrapping phase projection data and an algorithm that automatically converts 5 degrees of freedom (including possible linear and angular motion errors) into an alignment algorithm [2]. Li, J. believes that optical diffraction tomography (ODT) is an effective label-free technique for quantitative refractive index imaging. It can monitor the internal three-dimensional (3D) structure and molecular composition of biological cells for a long time with minimal disturbance. However, the existing optical tomography methods usually rely on the interferometric configuration of phase measurement and complex mechanical systems for sample rotation or beam scanning. Therefore, during the data acquisition process, the measurement may be affected by phase errors from coherent speckle, environmental vibration, and mechanical errors. To overcome these limitations, he proposed a new ODT technology based on non-interfering phase retrieval and programmable lighting emitted from a light-emitting diode (LED) array. The experimental system is based on a traditional bright-field microscope. The light source is replaced by a programmable LED array, which can provide variable-angle quasi-monochromatic illumination with an angular range of $\pm 37$ degrees [3]. Lighter, W. believes that known spectrally constrained diffuse optical tomography (SCDOT) can improve the reconstruction of diffuse optical imaging. Constraining the reconstruction by coupling optical characteristics at multiple wavelengths can suppress artifacts in the resulting reconstructed image. In other work, L1 norm regularization has been shown to improve certain types of image reconstruction problems. Because of its sparsity promotion characteristics, it is robust to noise and can preserve the edges in the image. But since the L1 norm is not differentiable, implementation is not always that simple. He showed how to incorporate L1 regularization into SCDOT. He evaluated the application of three popular L1 regularization algorithms in SCDOT: Iterative Reweighted Least Squares Algorithm (IRLS), Alternating Direction Multiplier Method (ADMM), and Fast Iterative Shrinkage Threshold Algorithm (FISTA). He introduced an objective procedure to determine the regularization parameters in these algorithms and compare their performance in simulation experiments and real data obtained from the organization [4]. Through the ground penetrating radar implemented on the airborne platform, Gennarelli, G. has solved the problem of imaging shallow buried targets in surveys. The radar system is monostatic and collects scattered field data at a single frequency along parallel lines in the downward looking mode. The data is processed by an image forming algorithm based on the microwave tomography method. His method is valid under Born and start-stop approximations. The goal of his research is to obtain the analysis result of the spatial resolution based on the measurement configuration parameters. His results highlighted the special characteristics of the imaging configuration and provided useful instructions for setting up an appropriate acquisition strategy. Numerical results based on synthetic data are shown to support analysis of resolution limitations [5]. Demircan-Tureyen, E. believes that like many other linear inverse problems in the field of image processing, tomographic image reconstruction problems have an ill-posed nature. He developed the discrete tomography (DT) technology to solve this shortcoming by taking advantage of the discreteness of the image. Discrete Algebraic Reconstruction Technology (DART) is a DT technique that alternates between the inversion phase and the discretization (i.e., segmentation) phase in the algebraic reconstruction method (ARM). Total Variation (TV) minimization is another popular technique, which deals with the ill-posedness by using the piecewise constancy of the image, and the convex optimization problem needs to be solved. He proposed an algorithm that also performs continuous sequence inversion and discretization. But it is estimated that continuous reconstruction under TV-based regularization instead of using ARM. His algorithm combines the idea

of DART, which is to reduce the number of unknowns through subsequent iterations, and the setting based on 1-D TV [6]. Allag, A. believes that in many medical and industrial applications, accurate X-ray tomographic reconstruction of internal object structures is very important to obtain reliable interpretation data. In this context, he proposed a tomographic image reconstruction method based on FBP related to sinogram restoration. The restoration techniques he researched are based on first-order variational methods, such as the Chambolle-Pock algorithm. His method allows to improve the quality of tomographically reconstructed images with a reduced number of projections. Compared with the classic FBP reconstruction, the PSNR in the image is improved by 7 to 10 dB [7]. Tomography allows to obtain the spatial distribution of the internal material structure. Under certain experimental conditions, projection data collection is restricted by angles or guided by restricted angles. This requires sub-sampling of the number of projections or part of the data is missing. Therefore, the reconstructed image may suffer from severe artifacts, especially in the presence of noise. In the field of visual information, with the progress and development of society, people have higher and higher requirements for the quality of life. Vision has become an important part of humans' access to information. When the image that people observe is fuzzy and it is impossible to obtain beneficial information, it is usually because of the enlargement operation of the image with a small number of pixels, or because the image itself lacks the necessary high-frequency features, making the image texture inconspicuous.

Radon projection and reconstruction process is the main process of CT three-dimensional projection data generation. If a series of reconstructed tomographic images are stacked, a CT three-dimensional tissue structure is formed. In the three-dimensional space, the obtained two-dimensional sliced Biyun Temple architectural wood image is drawn by light projection. Perform trilinear interpolation on the original discrete data field and obtain the resampled data. Then, the data are classified and assigned, and shading calculations are carried out to draw, and a clearer equivalent surface Biyun Temple building wood image can be obtained. It can speed up the generation and transformation of Biyun Temple's architectural wood image. In this process, the resolution of wood images has great requirements. That is, the clearer the wood image, the higher the amount of information obtained by the computer, and the more accurate the wood recognition result. Due to the limitations of the existing imaging equipment, and the susceptibility to the influence and interference of external conditions in the image acquisition process, the acquired image usually contains noise or degradation, which makes the image look fuzzy subjectively.

## 2. Visualization Research Method of Scientific Calculation for Detecting Internal Defects of Wood

Through the comparison and comprehensive evaluation of various commonly used wood non-destructive testing methods, computer tomography, which is a branch of radiographic testing technology, is selected as the method of wood non-destructive testing. By comparing with traditional methods, the superiority of CT detection technology and the feasibility in practical application are explained. Biyun Temple is located in Xiaozhang Village. The temple buildings are built according to the terrain, increasing from south to north. The south side of the temple was originally a relatively open space, and the site of the original stage is located opposite the temple. From 2010 to 2011, a new stage and makeup building, and east and west corridors were built, and the newly built building walls were connected with the courtyard of Biyun Temple, forming a new courtyard and an old courtyard. The southeast is the village committee, and the northeast is the soil slope. The south, west, and north sides of Biyun Temple are paved roads in the village, and the roads on the three sides surround the temple [8]. Research on Biyun Temple to continue historical information such as history, science, artistic value, and humanistic sentiment. It preserves the continuity of its religious culture, makes it prolong its life, and provides real material materials for the study of early history, culture, and architectural art.

There are currently two entrances and exits in Biyun Temple, among which the mountain gate at the main entrance to the south of the temple has long been destroyed. It is now composed of iron gates and concrete steps. The east gate of the temple was built when it was used as a grain depot in the 1960s, and the temple can be accessed from two places. The temple buildings are built according to the terrain, gradually rising from south to north, forming the upper and lower courtyards. The lower courtyard is about 2.4 meters above the ground on the south side, and there are separate wing rooms and corridors on both sides of the courtyard. The upper court is about 2.3 meters higher than the lower court, and there is only one large hall in the courtyard. The building list of Biyun Temple is shown in Table 1.

The soil slopes on the east and west sides of the temple are eroded by rain all year round, and soil erosion has threatened the construction safety of Biyun Temple. The wires in Biyun Temple are not properly connected, and the wires are randomly laid on the buildings, posing a threat to the safety of cultural relics. The wooden components of the main hall of Biyun Temple are in disrepair for a long time, and there are many damages of different nature and different degrees. In addition to the deterioration and cracking of the individual components, especially the structure above the flat beam in the large wooden frame skews to the west, the serious deterioration of the four large-angle beams (one of which appeared to be broken) is the most serious of the fracture of the middle part of the stigma paving under the eaves and the deterioration of the eave pillar. The deteriorating situation of the big horn beam is shown in Figure 1. It can be seen that there are knots in the corner beam [9]. Using a computer to recognize wood is the smartest. The computer extracts data parameters, builds models, and distinguishes and recognizes the background program. When extracting data parameters, the resolution of the image is required to be higher. Using super-resolution reconstruction technology to improve the resolution of wood images can make wood recognition results more

Table 1: List of Biyun Temple buildings.

| Project | Years | Shape | Damage level |
|---|---|---|---|
| Mountain gate | 1990s | Two iron doors | — |
| East wing | Clear | It has four rooms wide, four rafters deep, and a single eave hanging from the top of the mountain | II |
| West wing | 1960s | It has four rooms wide, four rafters deep, and a single eave hanging from the top of the mountain | II |
| East gate | 1960s | One room wide, one rafter deep, and a single slope top | II |
| West mansion tent | 1980s | One room wide, one rafter deep, and a single eave hanging from the top of the mountain | III |
| East bungalows | Clear | It has three rooms wide, four rafters deep, and a hard top with a single eave | III |
| West bungalows | Clear | It has three rooms wide, four rafters deep, and a hard top with a single eave | II |
| Main hall | Five dynasties | It has three rooms wide, four rafters deep, and a single eave on the top of the mountain | IV |

Figure 1: The deteriorating situation of the big horn beam.

accurate. The so-called digital image processing is the use of digital computers or other high-speed, large-scale integrated digital hardware, by performing some digital operations or processing on the digital electrical signals converted from image information, in order to improve the quality of the image or achieve certain expected results required by people.

The principle of computer tomography (CT) is to reconstruct a two-dimensional cross-sectional image from rays using the information provided by an X-ray machine. Industrial computer tomography (ICT) is the extension and expansion of CT technology to the industrial field after its extensive success in the medical field. The structure of the ICT system is shown in Figure 2.

The formula of foreground depth $\Delta L_1$ is [10]:

$$\Delta L_1 = \frac{F\alpha L^2}{f^2 + F\alpha L}. \tag{1}$$

The formula of the background depth $\Delta L_2$ is [11]:

$$\Delta L_2 = \frac{F\alpha L^2}{f^2 - F\alpha L}. \tag{2}$$

The calculation formula of the depth of field $\Delta L$ is [12]:

$$\Delta L = \Delta L_1 + \Delta L_2 = \frac{2f\alpha L^2}{f^2 - F^2\alpha^2 L^2} \tag{3}$$

Suppose the spatial size corresponding to a pixel is $N$ (mm), then [13]:

$$\begin{aligned} M &= N, \\ N &= S/K. \end{aligned} \tag{4}$$

$S$ is the width of the field of view.

This research selects OK_M10A image capture card, OK_M10A is a standard black, and white video capture card based on PCI bus. It is the second-generation product of the OK series, an upgraded version of OK_M10A, and it covers most of the functions of OK_M80. OK_M10A is a universal high-quality image capture card suitable for image processing systems in scientific research, industrial inspection, etc. The video analog signal is input as a capture card, filtered, and A/D converted into 8bits digital signal. The image acquisition has high precision and small errors in the digital video signal after A/D conversion. It is suitable for high-precision and high-speed industrial detection and serial image processing research and development fields. The transfer speed of the image card is up to 25 MB/s, which can realize the reliable real-time transfer of the camera image to the computer memory. It continuously collects images of adjacent frames, accurate to the frame [14].

Twelve sensors are evenly arranged on a certain plane of the Biyun Temple log sample. The pendulum percussion device is used to make the pendulum strike the sensor in order with an impact swing angle of 10 degrees to generate a stress wave. When the source sensor is knocked, the remaining target sensors receive the stress wave at the same time. For the propagation time within the cross-section of the log sample, the ARBOTOM software system automatically calculates the propagation speed based on the distance between the sensors and the propagation time of the stress wave. After tapping the 12 sensors in clockwise order, the two-dimensional stress wave image of the cross-sectional information can be obtained. In the experiment, the same sensor should be tapped multiple times until the error of the stress wave propagation time data collected by the system is less than 5%; generally 4-6 taps are appropriate. After

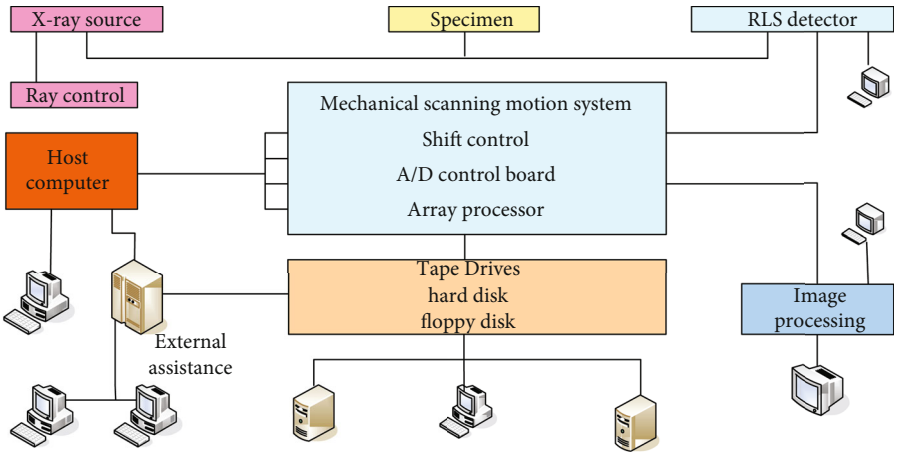


Figure 2: ICT system composition structure.

acquiring a cross-sectional stress wave tomographic image, the sensors are arranged again at an interval of 3 cm, and the experimental process is repeated. A set of 12-layer tomographic images were obtained on the same log sample, and the distance between each layer was 3 cm.

When the log propagates in the axial direction, the movement process of the tiny unit can be used for analysis. The force on interface $A$ is [15]:

$$P_A = \alpha \times S. \tag{5}$$

The force on interface $B$ can be described as [16]:

$$P_B = \left(\varepsilon + \frac{\partial \beta}{\partial x} dx\right) S. \tag{6}$$

According to Newton's second law, there are [17]:

$$\begin{aligned} ma &= P_B - P_A - F, \\ \rho \cdot S \cdot dx \cdot \frac{\partial^2 u}{\partial t^2} &= \left(\sigma + \frac{\partial^2 u}{\partial t^2} dt\right) - \sigma S - \mu \frac{\partial^2 u}{\partial x^2} dx, \\ \rho \cdot S \cdot dx \cdot \frac{\partial^2 u}{\partial t^2} &= \frac{\partial \alpha}{\partial x} S - \alpha S - \mu \frac{\partial^2 u}{\partial x^2} dx. \end{aligned} \tag{7}$$

According to Hooke's Law [18]:

$$\sigma = E \cdot \varepsilon = E \cdot \frac{\partial u}{\partial x}. \tag{8}$$

So,

$$\rho \cdot S \cdot dx \cdot \frac{\partial^2 u}{\partial t^2} = E \frac{\partial^2 u}{\partial x^2} \cdot dx - \mu v dx. \tag{9}$$

Both ends of the tiny element are free ends, and the strain at both ends of the log is zero. Therefore, the boundary condition of the movement of the tiny unit is [19]:

$$\frac{\partial u}{\partial x}|_{x=0} = \frac{\partial u}{\partial x}|_{x=dx} = 0. \tag{10}$$

Finally, it is concluded that the stress wave propagates in the horizontal direction [20]:

$$\frac{\partial^2 u}{\partial t^2} = c^2 \cdot \frac{\partial^2 u}{\partial x^2} - b \frac{\partial u}{\partial t}. \tag{11}$$

The constant $C_n$ in the formula is [20]:

$$C_n = \frac{2L}{N\pi} \cdot \frac{F_0}{S \cdot E} (\cos n \cdot \pi + 1). \tag{12}$$

The preprocessing of the image is realized by adopting the method of grayscale transformation and Gaussian filtering [21]. In digital image processing, the step of image grayscale transformation occupies a very important position. The sample images collected in this study are all color images, but processing the color images will increase the workload. At present, before performing pattern recognition and classification tasks, the image is generally converted into a grayscale image to facilitate the later feature extraction of the image. The essence of converting a color image into a grayscale image is to map the color components of each channel in the R, G, and B of the color image to a single grayscale value. This paper adopts the grayscale transformation based on the weighted average method [22, 23].

The mathematical expression of the weighted average method is as follows:

$$f(i,j) = W \cdot R(i,j) + W_g \cdot G(i,j) + W_b \cdot B(i,j). \tag{13}$$

In the formula, $f(i,j)$ represents the value of the grayscale image at the pixel point $(i,j)$.

The mathematical expression of Gaussian filtering is as follows:

$$G(m,n) = \frac{1}{2\kappa} e^{-\frac{x+y}{\phi}}. \tag{14}$$

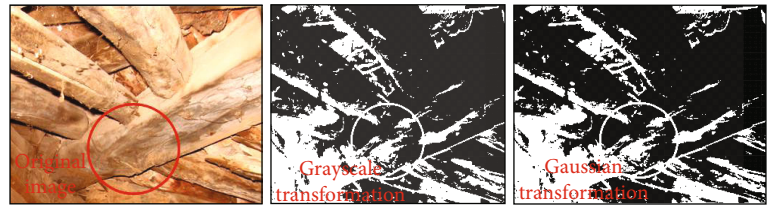


Figure 3: The final result of image preprocessing.


Figure 4: Comparison of segmentation of different algorithms.

Gaussian filtering is a linear smoothing filter, suitable for eliminating Gaussian noise, and is widely used in the denoising process of image processing. In layman's terms, Gaussian filtering is the process of weighted averaging the entire image. The value of each pixel is obtained by weighted average of its own and other pixel values in the neighborhood [24]. The specific operation of Gaussian filtering is to scan each pixel in the image with a template (or convolution, mask), and use the weighted average gray value of the pixels in the neighborhood determined by the template to replace the value of the center pixel of the template. The final result of image preprocessing is shown in Figure 3.

Define the membership degree of the neighboring pixel area:

$$\alpha(N(f(m,n))) = 1 - \frac{|N(f(m,n)) - f(m,n)|}{2}. \quad (15)$$

In the formula, $n$ is the number of bits of the gray image.

Let $g(f(i,j))$ denote the gradient of the gray value at pixel $(i,j)$, and define the following gradient boundary membership function.

$$\chi(g(f(i,j))) = g(f(i,j))/\max\,(g(f(i,j))). \quad (16)$$

The boundary membership degree is obtained by the compound operation of the neighboring pixel area membership degree and the gradient boundary membership degree. Here, multiplication is used to combine two degrees of membership, namely:

$$\eta(f(m,n)) = \alpha(f(m,n)) \times \gamma(g(f(m,n))) \quad (17)$$

The boundary points are marked as processed points. Then, find a new boundary point among the neighboring points of this boundary point, and calculate the neighboring point area membership degree and gradient boundary membership degree of each neighboring point of the known boundary point. And from this, the boundary membership degree of each neighboring point is derived, and then the new boundary point is judged by the principle of maximum membership degree. By analogy, until the closed boundary of area A is found. If there are holes in the area to be divided, repeat the operation to find other boundary lines of area A. The gray values of points other than the points included in these boundary lines are all set to the gray value of the background. In this way, area A is divided. The comparison of different algorithm segmentation is shown in Figure 4. It can be seen from the experimental results that the segmentation algorithm based on fuzzy theory proposed in this paper can get better segmentation results, and the boundaries of the segmented regions are clear. Usually images need to go through several steps to process: image enhancement, image segmentation, feature extraction, and pattern recognition and understanding. In the process of imaging defects on wood surface, due to various noises, such as salt and pepper noise, Gaussian noise, and Poisson noise, as well as interference from the on-site environment, the digital image obtained by the imaging device must undergo image enhancement processing. That is, it needs to filter and denoise the image, and it also needs to ensure that the image details are not lost as much as possible [25].

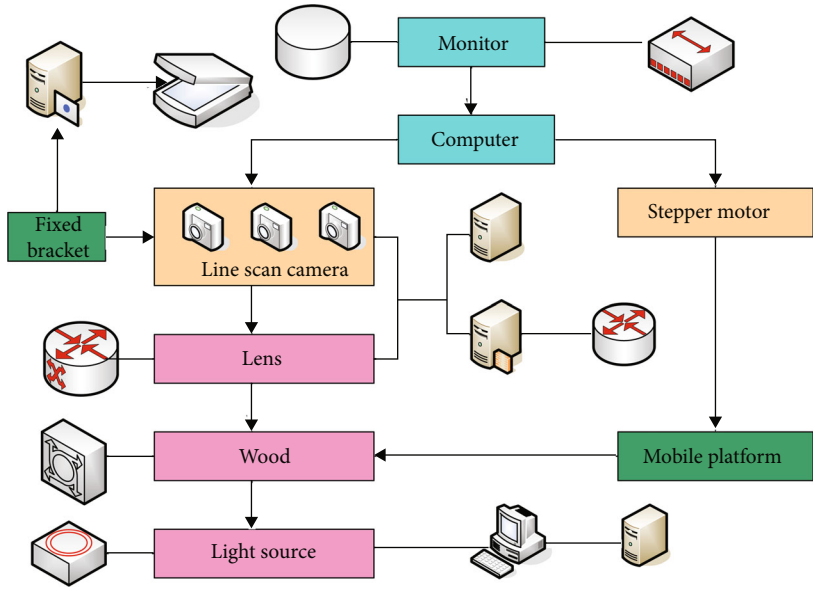


Figure 5: Three-dimensional visualization.

The three-dimensional visualization process mainly includes the five processes of CT three-dimensional data generation, data processing, visualization mapping, three-dimensional rendering, and display.

(1) The basic principle of CT is to irradiate each layer of wood with X-rays at multiple angles. According to the different degrees of absorption of rays by different tissues in the wood, the remaining rays after penetrating the cross-section of the wood are collected on the detector on the other side of the wood, and the projection data are obtained by arranging and sorting them. Then, use the reconstruction algorithm to reconstruct the projection data to recover the density function of the fault plane.

(2) Data processing: There are two main aspects of data processing. The first is to improve the quality of tomographic images. The most common operation is to eliminate the influence of noise. We know that CT will inevitably introduce noise during the projection process. In addition to a certain amount of noise reduction in the projection data, a certain amount of noise reduction is also required before the visualization reconstruction. Otherwise, the noise in the tomographic image will affect the visualization results. The second point is to appropriately simplify or supplement the original three-dimensional data field. At present, CT imaging technology can achieve scan spacing of 1 mm and below, and the resolution of each layer image is generally $256 \times 256$ and above, without excessive interpolation methods. On the contrary, for the relatively large CT three-dimensional data field, we have to filter and remove the redundant part. In general, the purpose of the data processing part is to improve the effect of CT 3D visualization and the reconstruction efficiency of 3D visualization.

(3) Visual mapping: The visual mapping step is the key operation in the entire visualization process. This step maps the three-dimensional data processed in the previous step into geometric figures and patterns that can be actually drawn. In this process, we need to decide what is finally presented and in what way. It includes various attributes such as the final geometry, color, and brightness. It makes the final drawn result meet the actual requirements.

(4) Three-dimensional rendering: The process of three-dimensional rendering is to organize the geometric figures and styles obtained in the previous step into displayable images. The rendering process mainly uses the technology of computer graphics, such as affine transformation, light intensity calculation, and display and hide.

(5) Display: As the last step in the visualization process, display is the display and geometric transformation of the output image, such as color quantization, image dynamic output, rotation, translation, and scaling

VTK (Visualization Toolkit) is an open source, freely available software system developed by Kitware. It is used for 3D computer graphics, image processing, and visualization.

Data input module: It is mainly responsible for reading CT tomographic data into the memory, including a variety of common formats such as Dicom, BMP, JPG, PNG, and TIFF. It mainly uses vtkDICOMImageReader, vtkImageReader, etc. in VTK. The encapsulation class supports multiple formats, and sets the corresponding data source path, the interval between slices and pixels, the resolution of slice pictures, and the number of slices.

Visualization algorithm module: Aiming at the Marching Cube algorithm (also known as the moving cube algorithm), experiments are performed on the visualization of CT three-dimensional tomographic images. Therefore, the

Table 2: Damaged status of the main hall.

| Number of starting contour vertices | Number of end contour vertices | Interpolation time (ms) | Damaged status |
|---|---|---|---|
| Main hall | Roof | Tile surface, ridge decoration | About 40% of the roof tiles were damaged. About 60% of the ridge is missing. 4 sets of beasts are missing. |
| | | Watching board, rafter, flying, hanging fish, wind board | About 80% of the wooden lookboard is decayed, and about 70% of the rafters are decayed. |
| | Wall | Surrounding walls | The front wall is about 6 square meters. The Liangshan brick wall is about 8 square meters, and the inner wall of the Liangshan wall is hollow and cracked about 70%. The lower sill wall of the inner wall of the back wall is about 2 square meters. |

core algorithm in this module will use vtkMarchingCubes to realize the selection of isosurfaces, and the isosurface constants need to be set. In addition, the experiment also used vtkDecimatePro to redundantly compress the isosurface data to reduce the amount of data read. vtkStripper connects the isosurfaces, and it also uses vtkSmoothPolyDataFilter to smooth the data to make the final drawn isosurfaces smoother.

Rendering and display module: The rendering and display module includes the newly created actor of vtkActor. At the same time, it sets the color, reflectivity, light intensity, and other attributes. It uses vtkCamera to adjust the angle of view and camera position. Finally, put the renderer with actors in the rendering window for drawing. After the drawing is completed, various interactions such as rotation, translation, and zooming of the 3D model can be realized. The three-dimensional visualization is shown in Figure 5.

The objective analysis of the simulation results is to give an objective evaluation of the image resolution based on the data indicators through computer vision. Commonly used objective evaluation indicators include Peak Signal-to-Noise Ratio (PSNR), MSE, Structure Similarity Index (SSIM), and average gradient. At present, PSNR and SSIM are the most common and widely used indicators to measure image quality.

$$\mathrm{PSNR} = 10 \log_{10}\left(\frac{R}{\mathrm{MSE}}\right)^3. \tag{18}$$

MSE is the mean square error.

$$\mathrm{MSE} = \frac{1}{mn}\sum_{i=0}^{m-1}\sum_{j=0}^{n-1}[I(i,j) - K(i,j)]^2. \tag{19}$$

$m, n$ is the width and height of the image.

SSIM is a new standard that has emerged in recent years to measure the similarity of two images, based on the definition of the brightness term (The Luminance Term), the contrast term (The Contrast Term), and the structural term (The Structural Term).

$$\mathrm{SSIM}(x,y) = [L(x,y)]^{\alpha} \cdot [C(x,y)]^{\beta} \cdot [S(x,y)]^{\chi}. \tag{20}$$

The definitions of $[L(x,y)]$ and $[C(x,y)]$ are as follows:

$$L(x,y) = \frac{\chi\kappa + C}{\chi^2 + \kappa^2 + C},$$
$$C(x,y) = \frac{\gamma\kappa + C_1}{\gamma^2 + \kappa^2 + C_1}. \tag{21}$$

## 3. Test Results of Internal Defects in Wood

Because of the eave pillars, the mountain surface and the rear eaves of the main hall are covered by the wall, and the beams are deformed and flashed in many places; the structural force changes. Part of the wall has been loaded, and the survey conditions are limited. During the survey, only a small area of the wall was excavated and surveyed. The damaged condition of the main hall is shown in Table 2.

The damage to the Donglang house is shown in Table 3.

The experimental results of Marching Cube are shown in Table 4. When the pixel block of the Marching Cube feature is $2 \times 2$, the recognition accuracy rate reaches 76%, which is higher than the recognition accuracy rate of the traditional LBP feature. This is because the Marching Cube feature can enhance the characterization ability of wood surface defects. But when the pixel block of the Marching Cube feature increases, the recognition accuracy will decrease. When the pixel block of the Marching Cube feature is $5 \times 5$, its recognition accuracy is 60.4%. This is because the pixel block size is too large, resulting in the loss of image information in the process of feature extraction. In addition, the training time of Marching Cube feature and LBP feature on the SVM classifier is maintained at about 24 s, and the feature dimension is 944 dimensions.

After using the key point extraction algorithm to simplify the contour of the known contour, it not only guarantees a good interpolation accuracy, but also greatly reduces the number of contour vertices. It greatly shortens the time used for interpolation and saves storage space. The number of contour vertices before and after the key points is extracted and the running time is shown in Table 5.

The average SSIM value of five images reconstructed by Marching Cube is 0.96 (the SSIM value of image processing using Bicubic interpolation, MAP, and OAI algorithm is shown in Figure 6(a)). It is 0.12 higher than the bicubic interpolation, the maximum posterior probability is 0.07,

Table 3: Damage to the East Corridor.

| Number of starting contour vertices | Number of end contour vertices | Interpolation time (ms) | Damaged status |
|---|---|---|---|
| East bungalows | Roof | Tile roof | The roof tiles are disjointed and loose, and the missing tiles are damaged by about 40% |
| | | Wood base | Even the eaves, roof tiles, and watch plates are all rotten, and the rafters are about 80% rotten. |
| | Wall | Surrounding walls | The wall soda is about 3 square meters, and there are some cracks. |

Table 4: Experimental results of Marching Cube.

| Feature | Feature dimension | Training time (s) | Accuracy (%) |
|---|---|---|---|
| LBP | 944 | 24.31 | 72.25 |
| Marching Cube $2 \times 2$ | 944 | 24.31 | 76 |
| Marching Cube $3 \times 3$ | 944 | 24.29 | 71.66 |
| Marching Cube $4 \times 4$ | 944 | 24.31 | 65.5 |
| Marching Cube $5 \times 5$ | 944 | 24.32 | 60.4 |

Table 5: The number of contour vertices before and after the key points are extracted and the running time.

| Contour | | Number of starting contour vertices | Number of end contour vertices | Interpolation time (ms) |
|---|---|---|---|---|
| Lin's example 1 | Key points not extracted | 208 | 238 | 16654 |
| | After extracting the key points | 46 | 56 | 1092 |
| Lin's example 2 | Key points not extracted | 117 | 137 | 5648 |
| | After extracting the key points | 26 | 33 | 541 |

the adaptive interpolation is 0.10, and the sparse representation is 0.04 (the SSIM value of image processing using Sparse, representation, and Marching Cube algorithms is shown in Figure 6(b)). Therefore, the super-resolution image obtained by Marching Cube has the least distortion.

The gray-level interpolation algorithm based on hypothesis test is stronger than the linear interpolation algorithm in three indicators, which proves that the algorithm in this section can get better results than linear interpolation. This algorithm not only considers the consistency of the gray value between the matching points, but also the consistency of the area near the matching points. The interpolation result obtained in this way is smoother. The comparison of the results of different grayscale interpolation algorithms is shown in Table 6.

After the original data is preprocessed, it is read into a specific array or octree. Extract a hexahedron from the mesh data volume and become the current hexahedron. At the same time, obtain all the information of the hexahedron, such as the values of 8 vertices and coordinate positions. Compare the function values of the 8 vertices of the current hexahedron with the given equivalent face value C, and get the state table of the hexahedron. According to the current state table index of the hexahedron, find the edge of the hexahedron that intersects with the isosurface, and use the linear interpolation method to calculate the position coordinates of each intersection. Using the central difference method, find the normal vectors of the 8 vertices of the current hexahedron. In the method of linear interpolation, the normal direction of each vertex of the triangle surface is obtained. According to the coordinates of the vertices of each triangle, the normal vector of the vertex connects the triangles.

When the noise variance is 0.0001, the noise component is present but not serious (the signal-to-noise ratio of the OPED reconstruction result is shown in Figure 7(a)). In this case, the signal-to-noise ratios obtained by the three methods are all around 30db. The Marching Cube algorithm proposed in this chapter is slightly higher than the other two methods. With the enhancement of the noise signal, the original OPED algorithm does not suppress the noise, and the reconstruction result deteriorates more drastically. When the noise variance reaches 0.01, the signal-to-noise ratio is only −13.397db. In the same situation, noise suppression is performed on the noisy Radon projection data, which greatly improves the reconstruction result. It can be seen from the line graph of the signal-to-noise ratio of Gaussian with OPED method and Marching Cube method (the signal-to-noise ratio of the Gaussian+OPED reconstruction result is shown in Figure 7(b)). As the noise increases, the signal-to-noise ratio of the reconstruction result becomes stable., Decrease gradually. Even if the noise variance

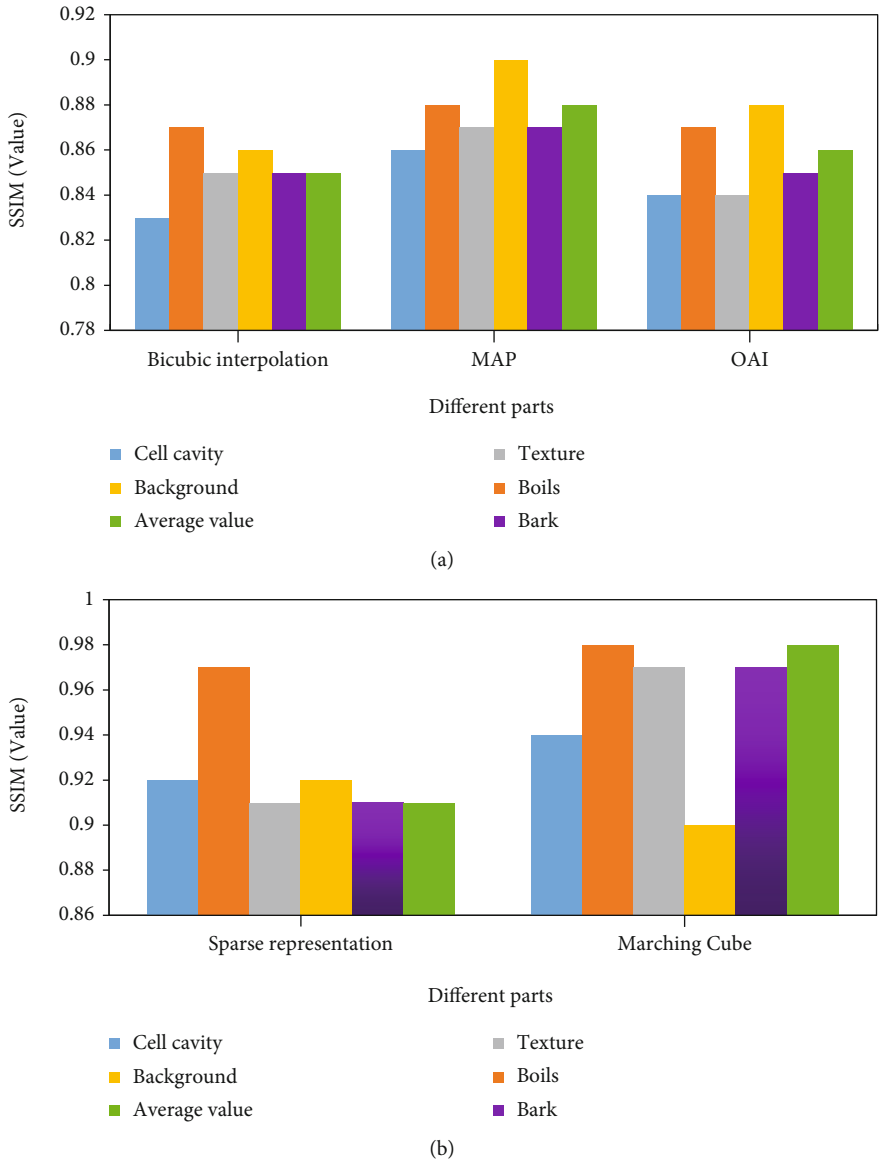


Figure 6: SSIM values of image processing by five different algorithms. (a) Bicubic interpolation, MAP, OAI. (b) Sparse, representation, Marching Cube.

Table 6: Comparison of results of different grayscale interpolation algorithms.

| Evaluation standard | The algorithm of this article | Linear interpolation algorithm |
|---|---|---|
| Mean square error | 50.76 | 62.49 |
| The total number of points with unequal gray values | 51172 | 76904 |
| Sum of absolute value of gray difference of all points | 4829057 | 6911538 |

reaches 0.01, the signal-to-noise ratio can be maintained at about 20db. In general, under different noise conditions, the signal-to-noise ratio of the Marching Cube algorithm is maintained at a relatively high level (the signal-to-noise ratio of the Marching Cube reconstruction result is shown in Figure 7(c)). It is about 3-4db higher than Gaussian's method of cooperating with OPED.

Different interpolation models have different requirements for the spatial characteristics of the sampling point set, and the accuracy of the interpolation under the same sampling point set is also different. When the sampling point set density is larger and the spatial features are simpler, the interpolation model can generally achieve higher interpolation accuracy. When the data point set is insufficient, the inverse distance weight interpolation model requires the sampling point set to be distributed on the feature points as much as possible. The regular spline interpolation model requires that the curvature between the sampling points is

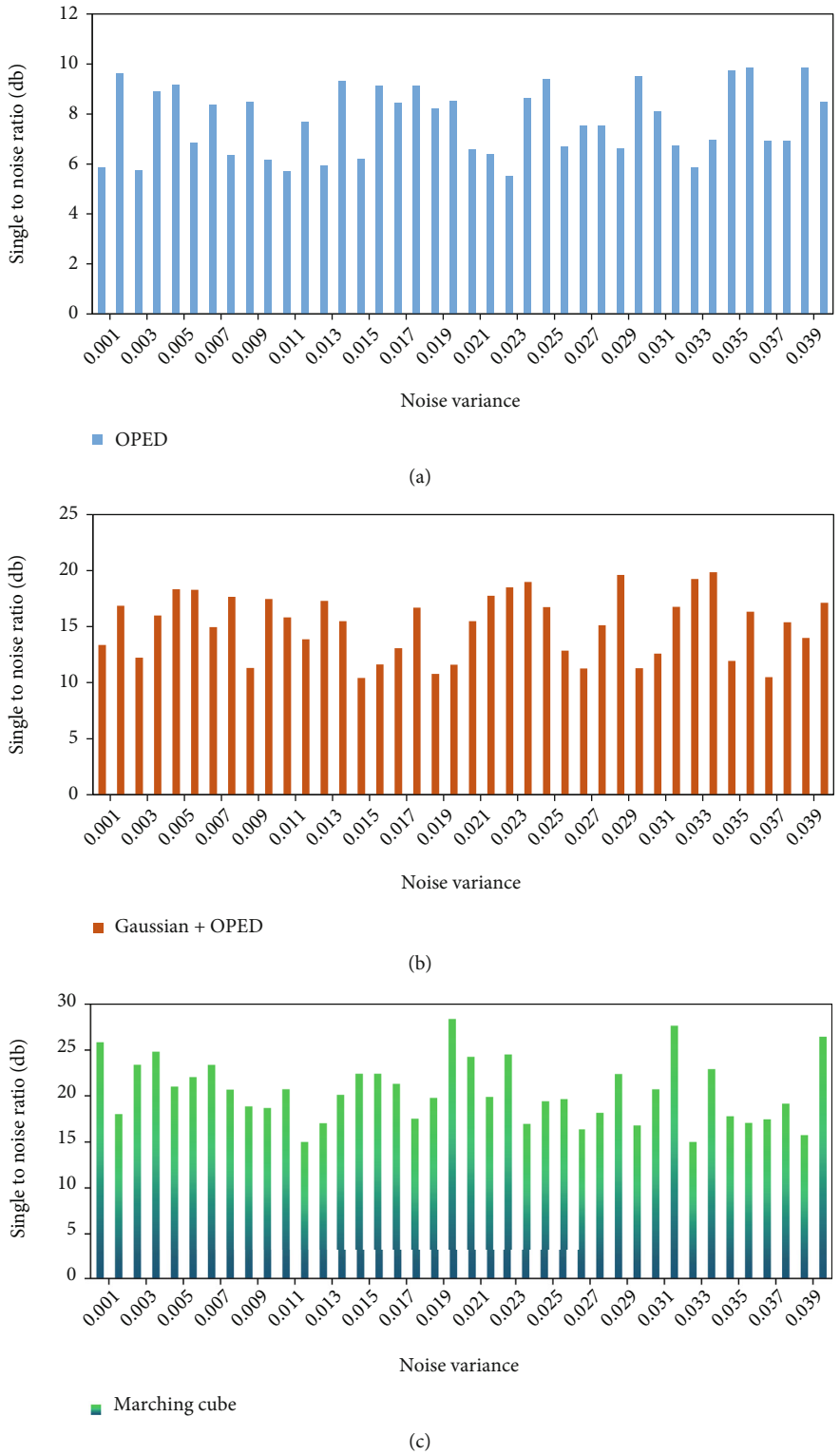


Figure 7: Comparison of the signal-to-noise ratio of the reconstruction results of the three reconstruction methods under different noise conditions. (a) OPED. (b) Gaussian+OPED. (c) Marching Cube.

small and the distribution is uniform. The ordinary Kriging interpolation model requires that the spatial characteristics of the sampling point set be analyzed first, and then the appropriate variation function is selected for interpolation according to the spatial characteristics.

Further analyzing of some pixels in the reconstruction results, here are, respectively, selected the 122nd row of pixels as the object to draw a line map. It can be found from the line graph 8 that the reconstruction results of the two algorithms are roughly consistent with the original image

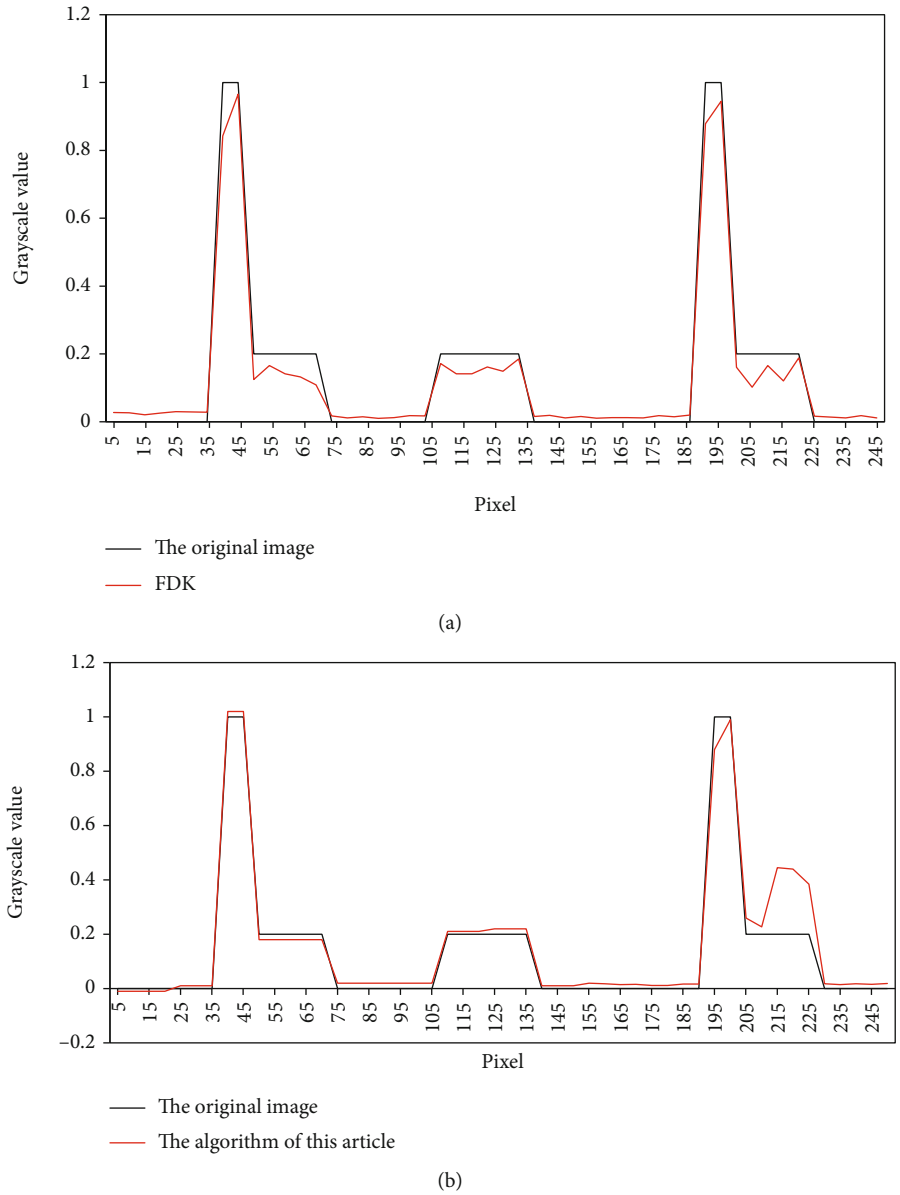


Figure 8: Analysis of some pixels in the reconstruction result. (a) The coincidence line between the original image and the FDK algorithm. (b) The line of coincidence between the original image and the fuzzy theory image segmentation algorithm proposed in this research.

(the line of coincidence between the original image and the FDK algorithm is shown in Figure 8(a)). Among them, the FDK algorithm result curve has certain fluctuations, and the fluctuation range is relatively large near the edge of the image. This result is consistent with the artifacts observed in the previous partial enlarged images. The algorithm proposed in this paper can fit the original curve better, and the fluctuation is small (the line of coincidence between the original image and the fuzzy theory image segmentation algorithm proposed in this research is shown in Figure 8(b)).

Using image processing to detect wood defects will provide theoretical guidance for the development of intelligent board defect recognition machines. It solves the problem of large errors in manual identification of wood defects and difficulty in double-sided identification, and brings huge economic benefits to the wood industry. And this article based on the existing digital image processing technology and artificial intelligence technology to identify the defect pattern, and then evaluate the material.

The roof base of Biyun Temple is mainly composed of straw, and the rafters are composed of logs. The recognition rate of straw and log means the amount that can be recognized by the straw and log sample using the mapping parameter divided by the total volume of the sample. The recognition rate indicates the strength of the parameter's recognition effect on straw and logs. The higher the recognition rate, the better the recognition effect. It can be seen from the recognition results that when the brightness MSE is used as the recognition parameter, the method in this paper improves the recognition rate of straw by 0.4% and the recognition rate of logs by 0.3% compared with the traditional method. When the angle MSE is used as the recognition

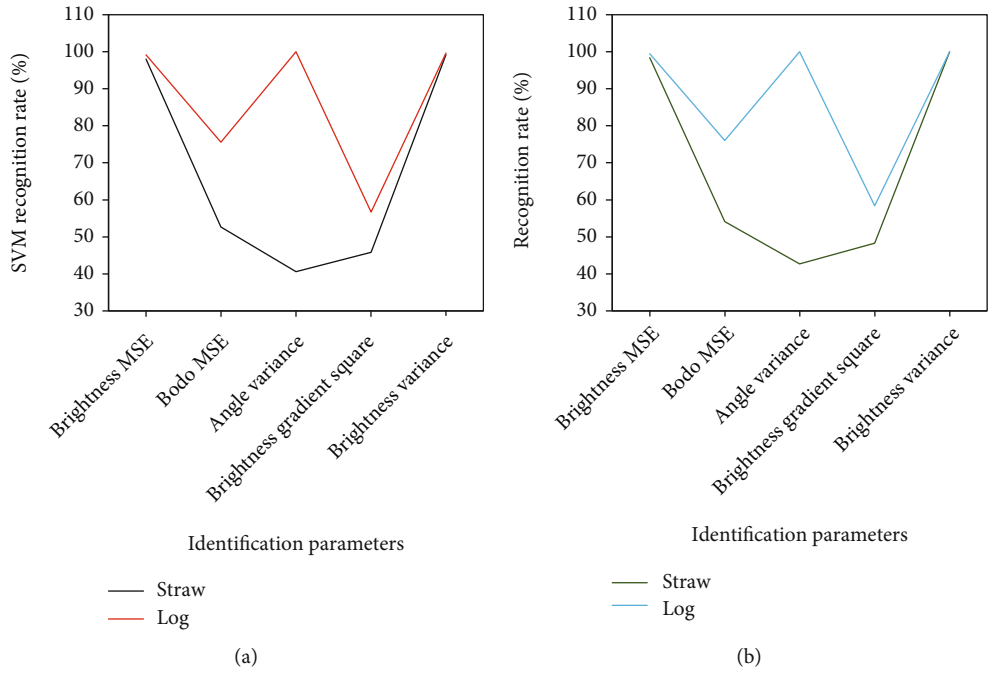


Figure 9: Recognition effect of different methods. (a) Traditional methods. (b) The method of this paper.

parameter, compared with the traditional method (SVM), the recognition rate of this method for straw is increased by 1.4%, and the recognition rate for logs is increased by 0.4%. When the angle variance is used as the recognition parameter, the method in this paper improves the recognition rate of straw by 2.1% compared with the traditional method. When the brightness gradient variance is used as the recognition parameter, the method in this paper improves the recognition rate of straw by 2.5% and the log recognition rate by 1.7% compared with the traditional method (the recognition effect of the traditional method is shown in Figure 9(a)). When the brightness variance is used as the recognition parameter, compared with the traditional method, the recognition rate of this method for straw is increased by 0.8%, and the recognition rate for logs is increased by 0.4% (the recognition effect of this method is shown in Figure 9(b)).

## 4. Discussion

There is a lack of historical materials about Biyun Temple, and there are few records about the historical structure and scale of the temple. When investigating the site, the villagers only learned that the existing layout of the temple has not changed significantly since the 1940s, and only the gate on the south side of the courtyard has been demolished. The original stage collapsed and destroyed in the 1970s. The temple sits on the north side and faces the south, and has two courtyards. The floor of the courtyard is paved with bricks, and the central axis is set with a corridor. The courtyard is high in the north and low in the south, and the precipitation flows naturally along the slope. The precipitation in the courtyard is collected at the east gate and discharged outside the courtyard at the southern end of the courtyard. The temple is located on a soil platform. Due to long-term rain erosion and lack of cleaning and maintenance, the outer slope of the courtyard is overgrown with weeds and shrubs, resulting in poor drainage. Soil erosion has gradually endangered the basic safety of cultural relics. The date when Biyun Temple was built is unknown. The existing main building hall is judged to be the remains of the Five Dynasties. The history is very long and the building is well preserved. It preserves the relevant historical information of early buildings and shows the development and changes of ancient wooden buildings. The existing buildings of different periods in Biyun Temple reflect the characteristics and artistic achievements of the architectural appearance, form, and decoration methods of different historical periods in the local area. It shows the technological level and development process of ancient local architecture. The degree of integration of the building layout plan and the orderly arrangement of auxiliary buildings reflect the basic characteristics of the traditional building group planning layout. The main hall has a very long history. Its architectural remains can fully show its own uniqueness, and it is one of the typical representatives of early local architecture, the planning and layout of the building groups, the different proportions of buildings in different eras, the differences in architectural shapes and forms. It embodies the design concepts and expression methods of buildings in different periods, and reflects the artistic achievements of buildings in different historical stages. Different beam frame shapes, dougong structures, and building proportions show the development and evolution of construction technology and craftsmanship in different periods in history. It preserves and records important construction technical data. Biyun Temple is a typical building group dominated by early wooden ancient buildings. Protecting and repairing the historical buildings of Biyun Temple can ensure the continuity of the value of its architectural cultural relics.

With the continuous development of science and technology and the continuous reduction of wood resources, this destructive detection method is no longer suitable for current protection of wooden components of ancient buildings. Non-destructive testing methods for wood defects are currently more popular. This refers to the detection of wood defects based on the characteristics of wood defects without damaging the wood. Image processing technology is to process and process image information to meet actual needs. Since the advent of CT, it has been widely used in many fields such as military aviation and industrial inspection. In the field of imaging, it is hailed as one of the most important medical diagnostic tools in the twenty-first century. Throughout the development of CT, CT reconstruction technology has always been the core and key of CT, and it is also a hot spot in academic research. This paper conducts research from the two major directions of CT reconstruction technology: projection data reconstruction and visualization reconstruction. In terms of projection data reconstruction, this article pays more attention to the understanding and elaboration of theoretical knowledge and the exploration and derivation of new algorithms. Based on the in-depth study of the two-dimensional reconstruction algorithm, this paper proposes a new orthogonal polynomial expansion reconstruction algorithm based on the unit cylinder domain. It realizes the reconstruction of the three-dimensional Radon projection data, and provides a projection data scanning strategy that matches the algorithm. From the perspective of 3D visualization reconstruction, this article focuses on practice. This paper tries to design and realize the current mainstream 3D visualization reconstruction technology with the help of existing visualization tools, and obtains a relatively satisfactory visualization rendering result.

## 5. Conclusion

In the sampling process, due to the interference of external factors, the constraints of imaging equipment and other uncertain factors, the resolution of the collected images is often not high, and even the normal viewing is affected. From the perspective of wood recognition, the unclear image details and the lack of texture pixels all affect the accuracy of computer recognition. The process of judging the wood defect image is mainly composed of the following parts: reading the image, filtering out the background, calculating the input and output flags, and resetting the flags. The initial sample image obtained by the camera includes not only the wood itself, but also the background area. The background area has a great interference effect on the recognition of veneer. The main function of judging the wood defect image is to remove the background area, while retaining the normal sample part. The main process of the system mainly includes the following parts: system initialization, the process of judging wood images, the judging process of wood defect image types, and the archiving process of identified wood information. This article introduces the system initialization and the process of judging wood images. The archiving process of wood image information is to archive the identified and unidentified wood defects, which is convenient for future query and so on. In terms of defect recognition, this article should use more methods for training, such as the use of fractal theory to improve the recognition rate and increase the recognition efficiency.

## Data Availability

The data used to support the findings of this study are available from the corresponding author upon request.

## Conflicts of Interest

The authors declare no conflicts of interest.

## Acknowledgments

The research work was supported by NFGA Standard Project (No. 2021-LY-062), CAF Science Fund (No. CAFYBB2021ZE004), and ——Research Institute of Wood Industry, Chinese Academy of Forestry (CAF), Beijing, 100091, China.

## References

[1] J. Chung and L. Nguyen, "Motion estimation and correction in photoacoustic tomographic reconstruction.," *SIAM Journal on Imaging Sciences*, vol. 10, no. 1, pp. 216–242, 2017.

[2] T. Ramos, J. S. Jrgensen, and J. W. Andreasen, "Automated angular and translational tomographic alignment and application to phase-contrast imaging,," *Journal of the Optical Society of America. A, Optics, Image Science, and Vision*, vol. 34, no. 10, pp. 1830–1843, 2017.

[3] J. Li, Q. Chen, J. Zhang, Z. Zhang, Y. Zhang, and C. Zuo, "Optical diffraction tomography microscopy with transport of intensity equation using a light-emitting diode array.," *Optics & Lasers in Engineering*, vol. 95, pp. 26–34, 2017.

[4] W. Lu, D. Lighter, and I. B. Styles, "L1-norm based nonlinear reconstruction improves quantitative accuracy of spectral diffuse optical tomography," *Biomedical Optics Express*, vol. 9, no. 4, pp. 1423–1444, 2018.

[5] G. Gennarelli, I. Catapano, and F. Soldovieri, "Reconstruction capabilities of down-looking airborne GPRs: the single frequency case," *Computational Imaging, IEEE Transactions on*, vol. 3, no. 4, pp. 917–927, 2017.

[6] L. Wen, L. Han, H. Zhou, and H. Zhuge, "Developing charring rate models for Chinese species based on the thermodynamic theory," *Wood Science and Technology*, vol. 51, no. 5, pp. 1117–1131, 2017.

[7] E. Demircan-Tureyen and M. E. Kamasak, "A discretized tomographic image reconstruction based upon total variation regularization," *Biomedical Signal Processing & Control*, vol. 38, pp. 44–54, 2017.

[8] A. Allag, A. Benammar, R. Drai, and T. Boutkedjirt, "Tomographic image reconstruction in the case of limited number of X-ray projections using sinogram inpainting," *Russian Journal of Nondestructive Testing*, vol. 55, no. 7, pp. 542–548, 2019.

[9] H. Zheng, X. Tuo, S. Peng et al., "An improved algebraic reconstruction technique for reconstructing tomographic gamma scanning image," *Nuclear Instruments & Methods in Physics Research*, vol. 906, pp. 77–82, 2018.

[10] L. Han, X. Zhao, H. Zhou, and X. Luo, "Comparison between allowable properties method and reliability analysis method to determine design values of visually graded Chinese larch 40 x 65 mm lumber," *BioResources*, vol. 11, no. 1, pp. 651–662, 2015.

[11] G. Wang, J. Zhou, Z. Yu, W. Wang, and J. Qi, "Hybrid pre-log and post-log image reconstruction for computed tomography," *IEEE Transactions on Medical Imaging*, vol. 36, no. 12, pp. 2457–2465, 2017.

[12] G. K. Gedik and O. Sari, "Influence of single photon emission computed tomography (SPECT) reconstruction algorithm on diagnostic accuracy of parathyroid scintigraphy: comparison of iterative reconstruction with filtered backprojection," *Indian Journal of Medical Research*, vol. 145, no. 4, pp. 479–487, 2017.

[13] N. Banduka, D. Tadic, I. Macuzic, and M. Crnjac, "Extended process failure mode and effect analysis (PFMEA) for the automotive industry: the FSQC-PFMEA," *Advances in Production Engineering & Management*, vol. 13, no. 2, pp. 206–215, 2018.

[14] J. M. C. Brown, U. Garbe, and D. Pelliccia, "Statistical image reconstruction for high-throughput thermal Neutron Computed Tomography," *Nuclear Instruments and Methods n Physics Research*, vol. 942, pp. 162396.1–162396. 6, 2019.

[15] C. Michail, G. Karpetas, N. Kalyvas et al., "Information capacity of positron emission tomography scanners," *Crystals*, vol. 8, no. 12, pp. 459–459, 2018.

[16] P. M. Meaney, S. D. Geimer, and K. D. Paulsen, "Two-step inversion with a logarithmic transformation for microwave breast imaging," *Medical Physics*, vol. 44, no. 8, pp. 4239–4251, 2017.

[17] T. Sun, R. Clackdoyle, J. H. Kim, R. Fulton, and J. Nuyts, "Estimation of local data-insufficiency in motion-corrected helical CT," *IEEE Transactions on Radiation & Plasma Medical Sciences*, vol. 1, no. 4, pp. 346–357, 2017.

[18] S. Ahmed and I. Hoque, "Investigation of the causes of accident in construction projects," *Journal of System and Management Sciences*, vol. 8, no. 3, pp. 67–89, 2018.

[19] S. A. Tsekenis and N. Polydorides, "Optical access schemes for high speed and spatial resolution optical absorption tomography in energy engineering," *IEEE Sensors Journal*, vol. 17, no. 24, pp. 8072–8080, 2017.

[20] D. M. Bappy and I. Jeon, "Modified simultaneous iterative reconstruction technique for fast, high-quality CT reconstruction," *IET Image Processing*, vol. 11, no. 9, pp. 701–708, 2017.

[21] V. Moslemi and M. Ashoor, "Introducing a novel parallel hole collimator: the theoretical and Monte Carlo investigations," *IEEE Transactions on Nuclear Science*, vol. 64, no. 9, pp. 2578–2587, 2017.

[22] Y. Zhong, H. Zhou, and L. Wen, "The effect of elevated temperature on bending properties of normal wood inside Chinese larch wood during fire events," *BioResources*, vol. 10, no. 2, pp. 2926–2935, 2015.

[23] B. R. Crawley, T. C. Baum, K. J. Nicholson, and K. Ghorbani, "Adaptive vector method for motion compensation in ultra-wideband coherent Doppler tomography," *IEEE Transactions on Microwave Theory and Techniques*, vol. 67, no. 11, pp. 4591–4598, 2019.

[24] P. Trampert, J. Vogelgesang, C. Schorr et al., "Spherically symmetric volume elements as basis functions for image reconstructions in computed laminography," *Journal of X-Ray Science and Technology*, vol. 25, no. 4, pp. 533–546, 2017.

[25] H. Kohno, Y. Tanji, K.'. Fujimoto, H. Kitajima, Y. Horikawa, and N. Takahashi, "Reconstruction of CT images using iterative least-squares methods with nonnegative constraint," *Journal of Signal Processing*, vol. 23, no. 2, pp. 41–48, 2019.